

Infrared-terahertz double-resonance spectroscopy of CH₃F and CH₃Cl at atmospheric pressureDane J. Phillips,¹ Elizabeth A. Tanner,² Frank C. De Lucia,³ and Henry O. Everitt⁴¹*Kratos-Digital Fusion, 4904 Research Drive, Huntsville, Alabama 35805, USA*²*IERUS Technologies, 2904 Westcorp Boulevard, Suite 210, Huntsville, Alabama 35805, USA*³*Department of Physics, The Ohio State University, 191 Woodruff Avenue, Columbus, Ohio 43210, USA*⁴*Charles M. Bowden Laboratory, Army Aviation and Missile RD&E Center, Redstone Arsenal, Alabama 35898, USA*

(Received 19 January 2012; published 16 May 2012)

A method for highly selective remote sensing of atmospheric trace polar molecular gases is described. Based on infrared-terahertz double-resonance spectroscopic techniques, the molecule-specific coincidence between the lines of a CO₂ laser and rotational-vibrational molecular absorption transitions provide two dimensions of recognition specificity: infrared coincidence frequency and the corresponding terahertz frequency whose absorption strength is modulated by the laser. Atmospheric pressure broadening expands the molecular recognition “specificity matrix” by simultaneously relaxing the infrared coincidence requirement and strengthening the corresponding terahertz signature. Representative double-resonance spectra are calculated for prototypical molecules CH₃F and CH₃Cl and their principal isotopomers from which a heuristic model is developed to estimate the specificity matrix and double-resonance signature strength for any polar molecule.

DOI: [10.1103/PhysRevA.85.052507](https://doi.org/10.1103/PhysRevA.85.052507)

PACS number(s): 33.20.-t, 33.40.+f

I. INTRODUCTION

Double-resonance (DR) techniques are widely used in all phases of optical spectroscopy, from ultrafast pump-probe and excitation correlation measurements in the ultraviolet, visible, and infrared (IR) spectral regions to investigations of molecular collisional physics in the microwave-microwave and infrared-millimeter wave regions [1–7]. Although wavelength-degenerate DR techniques provide some insight into the relaxation dynamics from a photoexcited state, wavelength-nondegenerate DR techniques—which rely on the ability to tune the frequencies of the pump and probe beams independently—provide greater insight into energy-transfer pathways and rates [8–11]. Sometimes, the limited frequency tunability of pump or probe sources limits the effectiveness of DR techniques. For example, optically pumped far-infrared lasers—which use a line-tunable CO₂ IR laser to excite a terahertz (THz) rotational population inversion in a low-pressure gas—are constrained by the rare coincidence (<100 MHz) between any CO₂ laser line and any molecular rotational-vibrational IR transition [12–14]. This rare coincidence forces optically pumped far-IR (OPFIR) lasers to operate on only a few THz frequencies per molecule, but as the gas pressure and corresponding IR and THz linewidths increase, greater tunability and spectral coverage are possible [15–20].

Recently, we have proposed that the IR-THz DR technique may be adapted for remote sensing of trace gases in the atmosphere if IR pulses of sufficiently short duration (~100 ps) can be generated [21]. In particular, it was shown that a 100-m-thick cloud of CH₃F with a uniform concentration of 1 ppm (~1-mTorr partial pressure) could be detected using a THz transceiver tuned to the frequency of the IR pump-induced THz DR signature. Detection occurs through the co-propagation of the IR pump and the THz probe beams through the trace gas cloud to a retroreflecting surface up to 1 km away. If absorbed by the trace gas, the pulsed IR pump beam briefly alters the absorption strength of the returned continuous-wave THz probe beam, and this repeating modulation may be detected at the pulse repetition frequency

of the laser. The actual sensitivity of this technique depends in a complex manner upon the IR and THz absorption coefficients of the molecule and the atmospheric water vapor content. Recognition specificity is achieved through the molecule-unique combination of IR pump coincidence frequency and the frequency of the pump-induced change in the THz signature. For a given molecule, only a few of its hundreds of IR rovibrational transitions are coincident with any CO₂ laser line, and each rare coincidence produces a unique pump-induced absorption change in a few of the hundreds of THz rotational transition frequencies. These two dimensions of recognition (IR pump and THz DR frequencies) comprise a “specificity matrix” whose sparseness can be used to identify an atmospheric trace gas remotely with enough spectral discrimination that even isotopomers may be distinguished.

One of the findings of that paper [21] is that the coincidence requirement between CO₂ laser and IR molecular transition is relaxed when the trace gas primarily collides with atmospheric pressure gases (see Fig. 1). Specifically, Fig. 2 indicates that the rovibrational IR linewidth of CH₃F evolves from a Doppler-broadened $\Delta\nu_D = 33$ MHz [half width at half maximum (HWHM)] for low-pressure operation (typical of OPFIR lasers) to a pressure broadened $\Delta\nu_P = 2.3$ -GHz HWHM when the same 1 mTorr of gas is in an atmosphere of N₂ and O₂ [22]. Moreover, the IR linewidth function changes from Gaussian to Lorentzian, meaning that the spectral overlap falls off less abruptly with frequency at atmospheric pressure. This broadening relaxes the pump coincidence requirement from those rovibrational lines within 66 MHz of a CO₂ laser line [spaced 24–69 GHz apart, see Fig. 1(a)] to those within 4.6 GHz [23]. The benefit is that favorable IR-THz pump-probe combinations, including transitions that are not accessible at low pressure, may be selected for atmospheric remote sensing.

In order to explore the molecule-unique signatures that constitute the recognition specificity matrix, we calculate the double-resonance signatures of all IR-THz pump-probe coincidences at atmospheric pressure for ¹²CH₃F and CH₃³⁵Cl

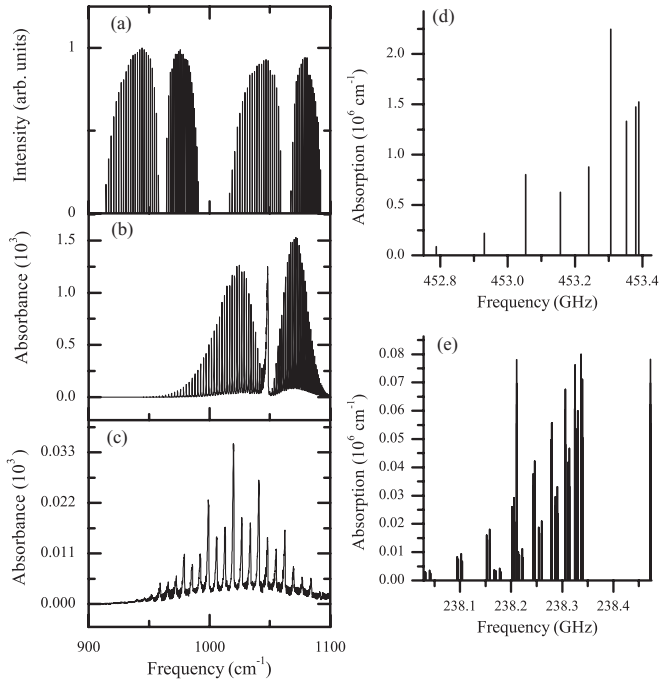


FIG. 1. Infrared spectra of (a) CO₂ laser [23], (b) CH₃F, and (c) CH₃Cl [28,38] between 900 and 1100 cm⁻¹. Rotational THz spectra of (d) $J = 8$ to 9 in $V_3 = 1$ of CH₃F and (e) $J = 8$ to 9 in $V_6 = 1$ of CH₃Cl.

and their principal isotopomers ¹³CH₃F and CH₃³⁷Cl that are 1% and 24% abundant, respectively. These molecules were chosen as prototypical because their excited vibrational levels are well isolated but different in nature: A CO₂ laser that is line tunable over a 9–11- μ m wavelength region (900–1100 cm⁻¹) excites the V_3 stretching mode of CH₃F and the V_6 bending mode of CH₃Cl. We show that the DR signatures are dramatically different for these two types of vibrational states in ways that are unique to the molecule, providing additional

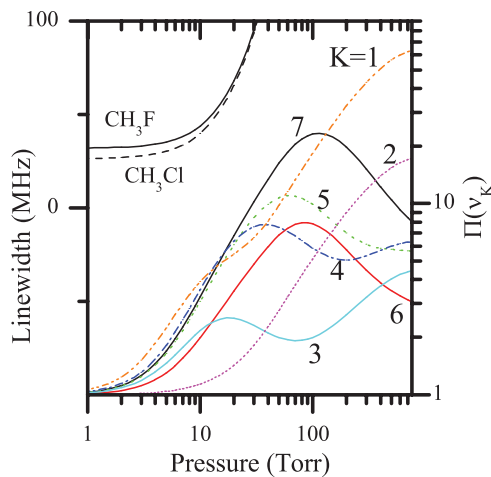


FIG. 2. (Color online) The calculated $\Pi(v_j)$ for each $Q_K(12)$ transition of ¹²CH₃F pumped by the 9P(20) CO₂ laser line, overlaid by the HWHM linewidth of IR rovibrational transitions of continuous lines: CH₃F, and dashed lines: CH₃Cl, from 1 to 760 Torr.

recognition specificity. Because many new coincidences occur at atmospheric pressure, we show how to estimate the strength of the DR signals so that the IR-THz combinations most useful for remote sensing may be identified.

II. DOUBLE-RESONANCE SPECTROSCOPY

A. Pump coincidences

The energy levels of the ground and excited vibrational states of CH₃F and CH₃Cl were calculated using the rotational constants listed in Tables I and II. For CH₃F, the standard P -type ($\Delta J = -1$), Q -type ($\Delta J = 0$), and R -type ($\Delta J = +1$) transitions from ground state to the V_3 vibrational level produce a classic stretching mode spectrum [Fig. 1(b)] whose absorption strengths are determined by a combination of the ground state's fraction of the temperature-dependent partition function, quantum-mechanical transition matrix element (Table III), and dipole derivative for the vibrational transition. The notation for a rovibrational transition is $X_K(J)$, where J, K designate the rotational state of the origin in the ground vibrational level and $X = P, Q, \text{ or } R$ depending on the type of rovibrational transition excited.

By comparison, the spectrum of the V_6 bending mode is characterized by l doubling that couples the bending motion $l = \pm 1$ with the rotation designated by the K quantum number. The notation is modified to $^Y X_K(J)$ to account for whether the rovibrational transition excited in V_6 satisfies $l = +1$ ($Y = R$) or -1 ($Y = P$). The corresponding spectrum [Fig. 1(c)] is remarkably different than for the bending mode in CH₃F because l doubling breaks the $\pm K$ degeneracy, dramatically affecting the energy-level structure and transition matrix elements (Table III). An examination of a partial low-pressure rotational spectrum of these two excited states [Figs. 1(d) and 1(e)] shows the effects of l doubling and hyperfine splitting in CH₃Cl. (Hyperfine splittings in CH₃Cl that are resolved at low pressure may be ignored at the atmospheric pressures of interest here.)

Using these calculated energy levels, the allowed IR rovibrational transition frequencies were calculated and were compared with the known frequencies produced by line-tunable CO₂ lasers [23]. To find nearly overlapping coincidences, assume for the moment that the IR pump is a continuous-wave CO₂ laser, so the coincidence occurs within the linewidth of the molecular rovibrational transition. For a pure 1-mTorr gas of CH₃F or CH₃Cl at 300 K, the salient IR rovibrational transition is Doppler broadened with a Gaussian HWHM linewidth $\Delta\nu_D$ of 33.4 and 27.4 MHz, respectively [24]. All rovibrational IR frequencies are then calculated, and the “offset” frequencies $\nu_{IR} - \nu_{\text{pump}}$ of those nearly coincident with specific CO₂ laser lines are compared with the values known from extensive research in OPFIR lasers [25,26]. The results, shown in Table IV, indicate the offset frequencies are in good agreement when the vibrational energies in Table I are used. As a notation to simplify the discussion, the rotational states connected by the pump are labeled (J_p, K_p, V_0) and (J'_p, K'_p, V_i) . The principal rotational transitions exhibiting THz DR signatures, involving the two pairs of adjacent rotational states $(J_p \pm 1, K_p, V_0)$ and $(J'_p \pm 1, K'_p, V_i)$, are labeled R_0^+ and R_0^-, R_i^+ , and

TABLE I. Molecular constants of methyl fluoride.

	$^{12}\text{CH}_3\text{F}$ [34]		$^{13}\text{CH}_3\text{F}$ [35,36]	
	$V_3 = 0$	$V_3 = 1$	$V_3 = 0$	$V_3 = 1$
A (MHz)	15 5352.70 (36) ^a	155 058.474 (19) ^a	155 365.345 (40) ^a	155 076.4480 (309) ^a
B (MHz)	25 536.149 80 (54) ^a	25 197.510 60 (87) ^a	24 862.665 (2) ^a	24 542.131 (3) ^a
D_j (kHz)	60.2214 (20) ^a	56.8868 (33) ^a	57.724 35 (1130) ^a	55.069 39 (1050) ^a
D_{jk} (kHz)	439.8156 (240) ^a	518.2386 (471) ^a	424.83 (11) ^a	477.773 (140) ^a
D_k (kHz)	2108.0 (75) ^a	2014.9000 (3358) ^a	2137.293 (1881) ^a	2071.5 (39) ^a
H_j (Hz)	-0.03214 (93) ^a	-0.193 20 (29) ^a	-0.021 30 (728) ^a	-0.1200 (66) ^a
H_{ijk} (Hz)	1.9470 (275) ^a	16.076 90 (5156) ^a	1.5360 (872) ^a	9.7025 (1510) ^a
H_{jkk} (Hz)	22.3610 (1601) ^a	-96.449 47 (48566) ^a	21.500 (764) ^a	-38.421 (1130) ^a
H_k (Hz)	0	0.119 7871 (22754) ^a	150.4 (2471) ^a	231.99 (138) ^a
L_j (mHz)	0	0.010 20 (87) ^a	0	0
L_{jjk} (mHz)	0	-1.7468 (187) ^a	0	-0.7732 (594) ^a
L_{jjkk} (mHz)	0	29.5648 (2138) ^a	0	13.300 (504) ^a
L_{jkkk} (mHz)	0	-173.2365 (14660) ^a	0	-89.64 (270) ^a
L_k (mHz)	0	0	0	0
Vibrational energy (cm ⁻¹)	-	1048.610 701 (10) ^a	-	1027.49320 (2) ^a
Dipole (debye) [31]	1.857	1.857	1.857	1.857
Dipole derivative (debye) [31]	-	-0.271	-	-0.271

^aUncertainties in the least significant digit(s) are in parentheses.

R_i^+ , respectively (see Fig. 3). The frequencies of these four rotational transitions are presented in Table IV.

Next, the rovibrational transitions of CH_3F or CH_3Cl with 1 mTorr of partial pressure are broadened by an atmosphere of N_2 and O_2 (i.e., concentration $\theta \sim 1$ ppm of analyte), and the coincidence calculation is repeated. Using a pressure-

broadening parameter of 3-MHz/Torr FWHM—typical for hard-shell collisions with nonpolar molecules [22]—the estimated linewidth of $\Delta\nu_p = 2.3$ -GHz HWHM far exceeds the Doppler-broadened linewidth. Using a Lorentzian line-shape function with this linewidth parameter, the overlap expands, and many new coincidences are found.

TABLE II. Molecular constants of methyl chloride.

	$^{12}\text{CH}_3\ ^{35}\text{Cl}$ [37]		$^{12}\text{CH}_3\ ^{37}\text{Cl}$ [37]	
	$V_6 = 0$	$V_6 = 1$	$V_6 = 0$	$V_6 = 1$
A (MHz)	156 051.1	156 810.71 (2) ^a	156 440	157 197.02 (3) ^a
B (MHz)	13 292.8752 (63) ^a	13 243.8840 (69) ^a	13 088.1660 (93) ^a	13 039.967 (10) ^a
D_j (kHz)	18.1010 (39) ^a	18.1360 (45) ^a	17.5630 (78) ^a	17.5960 (87) ^a
D_{jk} (kHz)	198.77 (13) ^a	203.37 (14) ^a	193.48 (13) ^a	197.85 (28) ^a
D_k (kHz)	2653.1	2735.2 (1) ^a	2501.0	2583.0 (1) ^a
H_j (Hz)	-0.008 45 (840) ^a	-0.010 10 (96) ^a	-0.0121 (20) ^a	-0.0140 (23) ^a
H_{ijk} (Hz)	0.312 (33) ^a	0.375 (36) ^a	0.312 (33) ^a	0
H_{jkk} (Hz)	9.53 (66) ^a	5.16 (72) ^a	8.39 (66) ^a	4.08 (190) ^a
H_k (Hz)	0	0	0	0
A_ζ (MHz)	0	39 275.246 (30) ^a	0	39 560.346 (33) ^a
q (MHz)	0	3.639 735 (250) ^a	0	3.580 87 (33) ^a
q_j (kHz)	0	-0.017 24 (10) ^a	0	-0.017 850 (17) ^a
q_{jj} (Hz)	0	0	0	0
η_j (MHz)	0	0.467 059 (78) ^a	0	0.457 777 (60) ^a
η_k (MHz)	0	4.027 59 (100) ^a	0	3.4039 (15) ^a
η_{jk} (kHz)	0	0.128 60 (57) ^a	0	0.1267 (10) ^a
η_{jj} (Hz)	0	-0.6601 (250) ^a	0	0
η_{kk} (kHz)	0	-0.1020 (45) ^a	0	-0.1250 (75) ^a
Vibrational energy (cm ⁻¹)	-	1018.071 10 (7) ^a	-	1017.695 45 (1) ^a
Dipole (debye) [31]	1.8989	1.8989	1.8989	1.8989
Dipole derivative (debye) [31]	-	-0.0388	-	-0.0388

^aUncertainties in the least significant digit(s) are in parentheses.

TABLE III. Branching ratios for transitions involving ground state (or stretching) and l -doubled bending vibrational states [30].

Ground, stretching transition	Branching ratio	l -doubled transition	Branching ratio
$P_K(J)$	$\frac{J^2 - K^2}{J(2J+1)}$	${}^R P_K(J)$	$\frac{(K-J)(K-J+1)}{4J(2J+1)}$
		${}^P P_K(J)$	$\frac{(-K-J)(-K-J+1)}{4J(2J+1)}$
$Q_K(J)$	$\frac{K^2}{J(J+1)}$	${}^R Q_K(J)$	$\frac{(J-K)(J+K+1)}{4J(J+1)}$
		${}^P Q_K(J)$	$\frac{(J+K)(J-K+1)}{4J(J+1)}$
$R_K(J)$	$\frac{(J+1)^2 - K^2}{(J+1)(2J+1)}$	${}^R R_K(J)$	$\frac{(J+K+1)(J+K+2)}{4(J+1)(2J+1)}$
		${}^P R_K(J)$	$\frac{(J-K+1)(J-K+2)}{4(J+1)(2J+1)}$

Table V lists only those coincidences in $^{12}\text{CH}_3\text{F}$ and $^{13}\text{CH}_3\text{F}$ whose overlap with the CO_2 laser is within one atmospheric pressure-broadened Lorentzian linewidth of the rovibrational center frequency. Of the new rovibrational coincidences that arise, many involve CO_2 lines that experience no low-pressure coincidences, whereas, the rest represent additional coincidences with CO_2 lines already known to have a low-pressure coincidence. In both cases, atmospheric pressure broadening of the rovibrational transitions often causes a given laser line to excite many rotational states simultaneously. The four rotational frequencies reported in Table V correspond to the rovibrational transition whose $(J_p, K_p, V_0) \rightarrow (J'_p, K'_p, V_i)$ transition most closely coincides with the strongest modulated terahertz absorption.

B. Differential absorption

The strength of the pump-induced THz DR signatures may be calculated from the standard equation for molecular absorption [24,27],

$$\begin{aligned} \alpha &= \frac{8\pi^3}{3hc} \nu (n_L - n_U) |\mu|^2 S(\nu, \nu_0) \\ &= 3.24 \times 10^{-6} \frac{\nu}{\Delta\nu} (f_L - f_U) \theta | \langle U | \mu_t | L \rangle |^2 \text{cm}^{-1}, \quad (1) \end{aligned}$$

where ν is the frequency (GHz) of the transition and $n_i = 2.45 \times 10^{13} f_i \theta \text{cm}^{-3}$ is the population of the molecular states connected by the probe and pump ($i = L, U$) for a nondegenerate fractional state population f_i and concentration θ ppm at 300 K in an ambient atmosphere of 760 Torr. The factor containing μ_t is the dipole matrix element for this transition (debye), and $S(\nu, \nu_0)$ is the lineshape function that simplifies to $1/\pi \Delta\nu$ (GHz^{-1}) at the peak

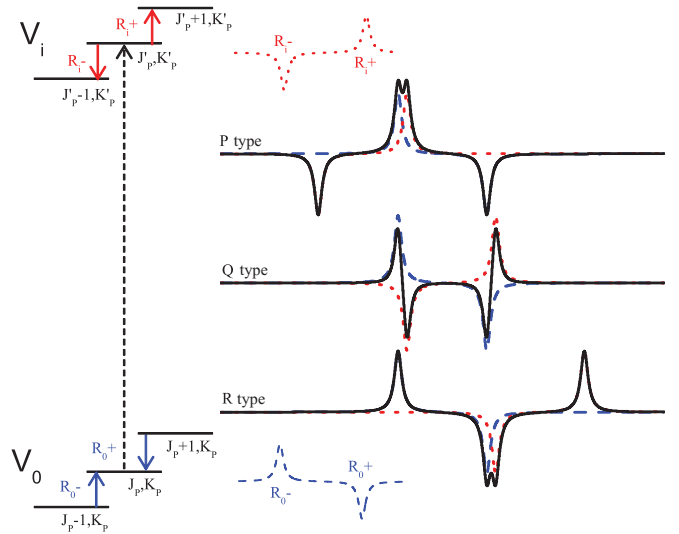


FIG. 3. (Color online) Energy-level diagram depicting black dashed arrow: the IR transition, and red and blue solid arrows: THz rotational transitions connecting the pumped states J_p, K_p , and J'_p, K'_p . The two pairs of THz DR signatures induced by the IR pump are illustrated for the dotted red line: V_i and dashed blue line: V_0 vibrational levels, the sum of which for the three types of IR transition (P, Q , and R types) produces the right: measurable DR signature.

of a pressure-broadened Lorentzian line shape [28,29]. The absorption α_{THz} at ν_{THz} arises from rotational transitions mediated by the permanent dipole moment of the molecule ($\mu_t = \mu$), whereas the absorption α_{IR} at ν_{IR} arises from rovibrational transitions mediated by the appropriate dipole moment derivative along the respective normal coordinate (Q_i) for the corresponding excited vibrational level ($\mu = d\mu/dQ_i$) [28].

Note that the absorption coefficient is proportional to the square of the appropriate dipole moment mediating the transition, multiplied by the rotational transition branching ratio $0 < | \langle U | \mu | L \rangle |^2 < 1$ given in Table III [30]. For IR transitions, the dipole derivative can be a factor of 10 (stretching modes) to 100 (bending modes) times weaker than the dipole moment itself, an effect that will tremendously affect DR spectroscopy. Specifically, $\mu = 1.86 \text{ D}$ and $d\mu/dQ_i = 0.2756 \text{ D}$ for the CH_3F V_3 transition, whereas, $\mu = 1.90 \text{ D}$ and $d\mu/dQ_6 = -0.0388 \text{ D}$ for the CH_3Cl V_6 transition [29–31]. Consequently, the IR transition absorption strength is approximately 2 orders of magnitude stronger in the stretching V_3 mode than in the bending V_6 mode. This difference arises because of the type of

TABLE IV. Optically pumped far-infrared laser coincidences for methyl fluoride and methyl chloride.

Molecule	Laser line	IR transition	IR transition offset (MHz)	R_0^- (GHz)	R_0^+ (GHz)	R_i^- (GHz)	R_i^+ (GHz)
$^{12}\text{CH}_3\text{F}$	9P(20)	$Q_2(12)$	39.78 [25]	612.409	663.365	604.297	654.582
$^{13}\text{CH}_3\text{F}$	9P(32)	$R_3(4)$	-24.25 [25]	198.855 [36]	248.559 [36]	245.350 [36]	294.406 [36]
$^{12}\text{CH}_3 \text{ } ^{35}\text{Cl}$	9P(26)	${}^R Q_3(6)$	20 [26]	159.477	186.050	158.894	185.370
$^{12}\text{CH}_3 \text{ } ^{35}\text{Cl}$	9R(12)	${}^R R_6(11)$	-30 [26]	292.190	318.733	317.569	344.009
$^{12}\text{CH}_3 \text{ } ^{37}\text{Cl}$	9P(38)	${}^R P_3(13)$	-50 [26]	340.093	366.227	312.806	338.850

TABLE V. Atmospheric pressure DR parameters for $^{12}\text{CH}_3\text{F}$ and $^{13}\text{CH}_3\text{F}$.

Laser line	IR transition	IR transition offset (GHz)	R_0^-	R_0^+	R_i^-	R_i^+
			ν_j (GHz)	ν_j (GHz)	ν_j (GHz)	ν_j (GHz)
			$\Delta\alpha(\nu_j)/\varepsilon$ (km $^{-1}$ kJ $^{-1}$)			
			$\Pi(\nu_j)$	$\Pi(\nu_j)$	$\Pi(\nu_j)$	$\Pi(\nu_j)$
$^{12}\text{CH}_3\text{F}$						
9P(18)	$Q_1(1)$	-2.135 {1} ^a		102.141 {1} ^a		100.786 {1} ^a
				-4.43		4.38
				0.27		0.25
9P(20)	$Q_{1:7}(12)$	0.042 {2} ^a	612.072 {6} ^a	663.000 {6} ^a	603.900 {6} ^a	654.152 {6} ^a
			61.03	-69.14	-60.22	68.22
			3.06	3.04	3.05	3.04
	$Q_{13}(13)$	-1.198 {13} ^a		712.291 {13} ^a		702.391 {13} ^a
				-1.61		1.59
				1.03		0.80
	$P_0(1)$	1.585 {0} ^a	51.072 {0} ^a	102.143 {0} ^a		50.395 {0} ^a
			7.64	-10.18		7.54
			1.90	1.00		1.93
9P(22)	$Q_{14:16}(18)$	0.0007 {15} ^a	914.385 {15} ^a	965.016 {15} ^a	901.451 {15} ^a	951.385 {15} ^a
			1.85	-2.41	-1.83	2.37
			1.77	1.74	1.74	1.72
$^{13}\text{CH}_3\text{F}$						
9P(08)	$R_{0:16}(20)$	0.535 {10} ^a	992.507 {3} ^a	1041.930 {3} ^a	1028.550 {3} ^a	1077.320 {3} ^a
			300.50	-315.75	-311.70	326.72
			4.49	4.62	4.60	4.46
9P(32)	$R_{0:4}(4)$	-0.025 {3} ^a	198.887 {0} ^a	248.598 {0} ^a	245.394 {0} ^a	294.458 {0} ^a
			112.30	-136.47	-134.71	158.70
			2.92	4.40	4.38	3.55

^aThe K quantum number of the transition closest to the CO_2 laser line is listed in curly brackets beside the IR transition offset frequency. The K quantum number of the transition with the lowest $\Pi(\nu)$ is listed in curly brackets beside the THz DR frequencies, and the values of $\Delta\alpha/\varepsilon$ and $\Pi(\nu)$ are only listed for these transitions.

motion involved, not because of the differing masses of the two molecules, suggesting a more universal insight: DR signatures are generally stronger in stretching modes than bending modes. Unfortunately, molecules tend to have more bending modes than stretching modes, which can be challenging if those modes span the region over which a CO_2 laser can be tuned.

The strength of the pump-induced THz DR signature may now be estimated. For an optically thin cloud ($\alpha_{\text{THz}}d < 1$) diluted in air to concentration θ with IR optical depth $\alpha_{\text{IR}}d < 1$, the total number of photons absorbed (i.e., the number of molecules photoexcited per pulse) is

$$N_{\text{pumped}} = \frac{\varepsilon}{h\nu_{\text{IR}}} \alpha_{\text{IR}} d, \quad (2)$$

where ε is the pump energy per pulse (J), d is the path length of the laser in the cloud, and α_{IR} can be calculated from Eq. (1) with the assumption $n_U \approx 0$. From this, it is easy to show that the fraction of the n_L molecules pumped per laser pulse in a beam of radius r_{IR} (m) is

$$f_{\text{pumped}} = \frac{\varepsilon \alpha_{\text{IR}}}{(\pi r_{\text{IR}}^2) (h\nu_{\text{IR}}) n_L} = 6.35 \frac{|(U| \frac{d\mu}{dQ} |L)|^2}{\Delta\nu_{\text{IR}} r_{\text{IR}}^2} \varepsilon, \quad (3)$$

where the transition matrix for this rovibrational transition is the product of the square of the corresponding dipole derivative (debye) and the appropriate transition branching ratio Table III.

These calculations assume there is no pump saturation, but for highly intense pump beams, saturation effects must be considered.

If the DR signature is observed on a time scale shorter than the collisional relaxation time (~ 100 ps at atmospheric pressure), then the only rotational transitions with photoinduced population changes are R_0^+ , R_0^- , R_i^+ , and R_i^- (Fig. 3). The pump-induced change in the absorption coefficients (1) arises from a change in the associated population differences from equilibrium ($n_L - n_U$) to pumped ($n_L \pm \Delta n - n_U$) values, where $\Delta n = N_{\text{pumped}}/V_{\text{IR}}$ and $V_{\text{IR}} = \pi r_{\text{IR}}^2 d$ is the volume occupied by the IR beam inside the gas. The measured THz DR spectrum is the pump-induced change in the rotational absorption coefficient,

$$\Delta\alpha = \pm \frac{8\pi^2}{3h^2c} \left[\frac{\nu_{\text{THz}}}{\Delta\nu_{\text{THz}}} |(U|\mu|L)|^2 \right] \times \left[\frac{\Delta\nu_{\text{IR}}}{\Delta\nu_{\text{IR}} + (\nu_{\text{IR}} - \nu_{\text{pump}})^2} \frac{\alpha_{\text{IR}}}{\nu_{\text{IR}} (\pi r_{\text{IR}}^2) \varepsilon} \right], \quad (4)$$

derived from Eqs. (1) and (2) as a product of terms that depend on the rotational transition (first bracket) and on the rovibrational transition (second bracket), where ν_{THz} corresponds to the monitored rotational transition with the indicated transition matrix element. Notice that a Lorentzian line-shape factor has been added to account for the reduced

IR absorption caused by the offset (reported in Table V) between the pump and the atmospheric pressure-broadened rovibrational transition frequencies. (Figure 2 indicates the pressure at which the Lorentzian line shape must be replaced by a Gaussian.) Because $\Delta\alpha$ grows linearly with IR pump energy (ε) per pulse, the DR absorption strengths are reported as $\Delta\alpha/\varepsilon$ in units of $\text{kJ}^{-1} \text{km}^{-1}$ in Table V.

C. Overlap enhancement

Since the THz rotational transitions undergo the same pressure broadening as the IR rovibrational transitions, the THz DR spectra of nearby pumped rotational transitions may also overlap. This overlap may strengthen or may weaken the THz DR signal from the low-pressure value Eq. (4) in which only one rovibrational transition is pumped. The multiplicative factor by which a given transition is strengthened or is weakened is significantly less than the number of overlapping transitions because the constituent line strengths may have differing degeneracies and thermal populations as well as overlaps with the opposite sign of $\Delta\alpha_j$. (For a given laser line, the overlapping transitions in CH_3F are labeled by the subscripts in the ‘‘IR transition’’ column of Tables IV and V.) The overlap enhancement factor in Table V,

$$\Pi(\nu_j) = \frac{\sum_{i=1}^n \Delta\alpha_i \frac{(\Delta\nu_p)^2}{(\nu_i - \nu_j)^2 + (\Delta\nu_p)^2}}{\Delta\alpha_j} \quad (5)$$

estimates how many times stronger or weaker the DR signal $\Delta\alpha_j$ will be at frequency ν_j because of the overlap from nearby DR features of strength $\Delta\alpha_i$ located at ν_i . Here, the summation is over all n DR signatures associated with all IR transitions excited by a given laser line where the $\Delta\alpha_i$ and $\Delta\alpha_j$ are calculated in Eq. (4). When the THz transitions overlap, the largest $\Delta\alpha_j$ necessarily produces the smallest value of $\Pi(\nu)$ at the transition labeled $\{R\}$, so this is the value provided in Table V. The peak of the summed DR signature will be near $\nu_{\{R\}}$, so this is the most appropriate frequency to use for the THz probe.

The product $\Delta\alpha_j \Pi(\nu_j)/\varepsilon$ represents the final estimate of the THz DR strength for a given IR-THz combination in the specificity matrix. This product can be used to ascertain which of the old or new coincidences are most promising for remote sensing for a given isotopomer. Remember that $\Delta\alpha_j \Pi(\nu_j)$, which may be positive or negative, represents a pump energy-dependent (ε) increase or decrease in the ambient THz absorption strength as $\alpha_{\text{THz}}(\nu_j) \rightarrow \alpha_{\text{THz}}(\nu_j) + \Delta\alpha_j \Pi(\nu_j)$. Although usually observed as a short-lived pump-induced change in absorption strength, THz emission can actually occur when $-\Delta\alpha_j \Pi(\nu_j) > \alpha_{\text{THz}}(\nu_j)$. Because atmospheric collisional redistribution of population is minimal on time scales shorter than 100 ps, $\Delta\alpha_j \Pi(\nu_j)/\varepsilon$ only depends on the absorption strength of the IR rovibrational molecular transition, the detuning of the spectral overlap with the nearest CO_2 laser line, and the aggregate strength of the overlapping rotational transitions involving states simultaneously excited by the laser [$\Pi(\nu_j)$]. Note that the absorption strength of the IR rovibrational transition depends on the type of vibrational mode for a given molecule (dipole derivative for stretching or bending modes), the specific rovibrational transition type

involved (branching ratios for P , Q , or R), and the rotational partition function (or more precisely, the ground rotational state population n_L of the pumped rovibrational transition). Not surprisingly, the optimal rovibrational transitions for DR spectroscopy are those with the strongest IR absorption, i.e., those nearest the peak of the IR spectrum.

Finally, it has already been pointed out that the pressure-broadened Lorentzian line-shape function falls off less abruptly than the Doppler-broadened Gaussian line-shape function, so overlaps are more readily excited. The decision to include only those overlaps within one linewidth $\Delta\nu_{\text{IR}}$ of the rovibrational line center was arbitrary. Recall the calculation assumed the CO_2 laser was operating continuously; however, if the laser was pulsed, the increased spectral bandwidth of the laser pulses should also be considered in the coincidence calculation. For the remote sensing application, pump pulses of durations comparable to the hard-shell gas kinetic collision time (~ 100 ps) are required, corresponding to a spectral bandwidth of 10 GHz that is (not coincidentally) comparable to the pressure-broadened linewidth $\Delta\nu_p$ of the IR rovibrational transition. Clearly, even more coincidences may be excited when such short pulses are used, but the pump efficiency is reduced by the fraction of pump radiation that falls outside the spectral bandwidth of the IR absorption line.

III. SPECIFIC EXAMPLES

Having outlined the basic principles underlying the excitation of a DR signal, we next explore the variety of DR signal types, their strengths, and how they depend on the type of photoexcited rovibrational transition (Fig. 3). Again, we restrict ourselves to photoexcitation on time scales short compared to the fastest collisional relaxation time of the molecule (~ 100 ps), so only rotational transitions R_0^+ , R_0^- , R_i^+ , and R_i^- are involved.

A. Methyl fluoride

We start with the simpler case, CH_3F , for which the stretching mode V_3 of both $^{12}\text{CH}_3\text{F}$ and $^{13}\text{CH}_3\text{F}$ isotopomers is photoexcited by a CO_2 laser. Considering first $^{12}\text{CH}_3\text{F}$, the $9P(20)$ line of a CO_2 laser is known to photoexcite the $Q_2(12)$ [and perhaps the $Q_1(12)$] transition at low pressure. The resulting DR signature has components at 612.409 (R_0^-), 663.365 (R_0^+), 604.297 (R_3^-), and 654.582 GHz (R_3^+). The absorption decreases ($\Delta\alpha_j < 0$) in transitions R_0^+ and R_3^- and increases ($\Delta\alpha_j > 0$) in transitions R_0^- and R_3^+ [Figs. 3 and 4(a)], illustrating that a characteristic Q -branch THz DR signature consists of four spectral features in the form of conjugate doublets (two R^- and two R^+) separated by $\sim 2B \approx 51$ GHz. Assuming there is no IR pump saturation, Eq. (4) indicates the strengths of these four DR features are linearly proportional to the pump pulse intensity, their THz frequency, and the associated branching ratios (Table III). Each doublet consists of the identical rotational transitions in V_0 and V_3 separated in frequency by $\sim 2(B_3 - B_0)(J + 1)$, a separation of 8.1 GHz for $J = 11 \rightarrow 12$ and 8.8 GHz for $J = 12 \rightarrow 13$. Given that $\Delta\nu_p = 2.3$ GHz, these four features are well resolved at atmospheric pressure.

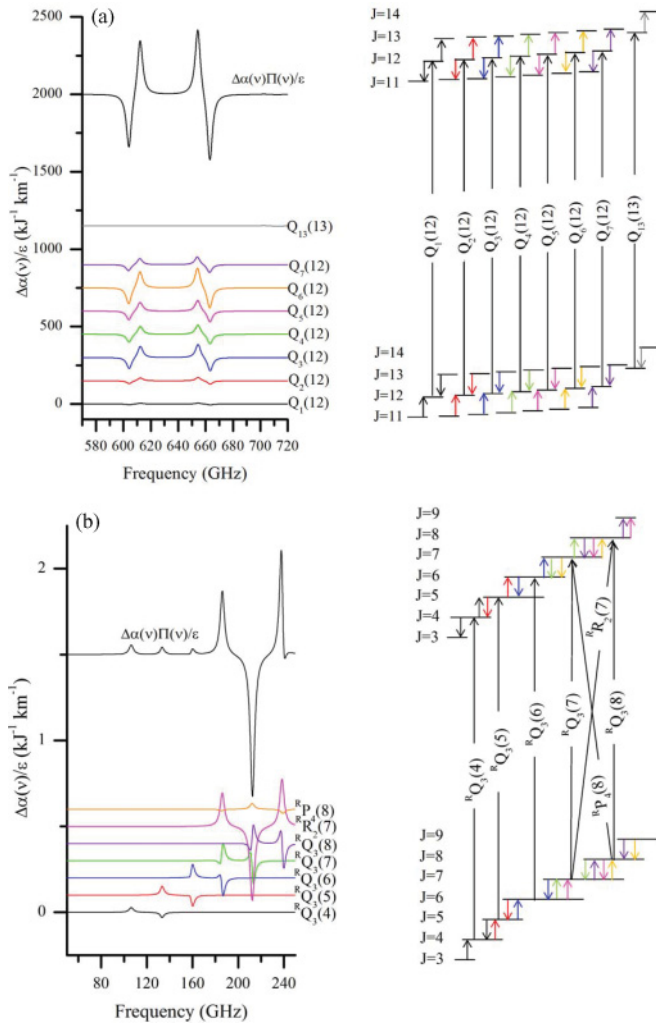


FIG. 4. (Color online) (a) Aggregate DR signature for the $^{12}\text{CH}_3\text{F}$ transitions pumped by the $9P(20)$ laser line, plotted above the constituent labeled components from Table V (to scale). Energy-level diagram depicting both infrared pump transitions and rotational transitions connected to the pumped states. (b) Aggregate DR signature for the $\text{CH}_3\ ^{35}\text{Cl}$ transitions pumped by the $9P(26)$ laser line, plotted above the constituent components (to scale) labeled center. Energy-level diagram depicting both infrared pump transitions and rotational transitions connected to the pumped states. The transitions $^P R_0(24)$, $^R R_0(24)$, and $^R P_7(31)$ from Table VI are not depicted because they occur at higher frequencies.

As noted above, the atmospheric pressure-broadened width of the rovibrational transitions allows a given laser line to photoexcite many neighboring transitions, primarily those transitions with differing K values, further increasing the strength of the DR signature. In $^{12}\text{CH}_3\text{F}$, the $9P(20)$ laser line now coincides with nine additional atmospheric pressure-broadened rovibrational transitions [$Q_1(12) - Q_7(12)$, $Q_{13}(13)$, and $P_0(1)$]. When a series of transitions with constant J but varying K are pumped [e.g., $Q_1(12) - Q_7(12)$], it is listed as a single entry in Table V with $\{R\} = \{K\}$ for the transition with smallest $\Pi(v_j)$. Figure 2 shows how the multiplier $\Pi(v_K)$ for each of the $Q_K(12)$ transitions ($K = 1-7$) grows with increasing pressure, and Figs. 4(a) and 5(a) show how their aggregate DR signature is the sum of all the constituent overlapping

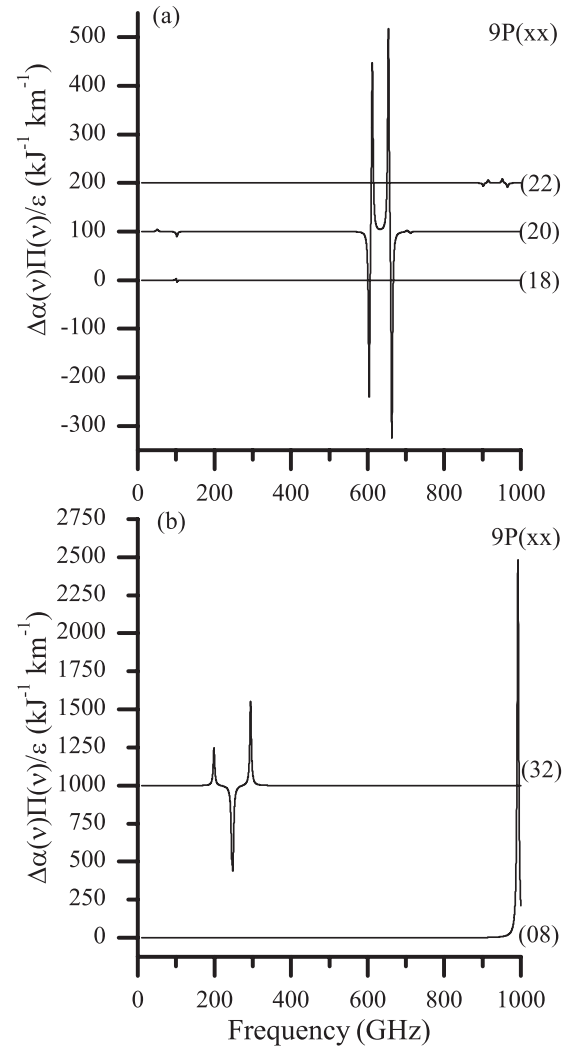


FIG. 5. Calculated DR signatures for all laser coincidences with (a) $^{12}\text{CH}_3\text{F}$ and (b) $^{13}\text{CH}_3\text{F}$. The coincident CO_2 laser lines are listed on the right.

Q -branch signatures for a portion of the THz region. Notice that $\Pi(v_j) = 1$ for $Q_2(12)$ until the pressure broadening exceeds the Doppler broadening of the IR transition, after which there is a rapid, often nonmonotonic growth in $\Pi(v_j)$ for all transitions as pressure increases. Notice $\Pi(v_j)$ for $\{K\} = 6$ only reaches 3.04 at atmospheric pressure, not the theoretical maximum of 6.15 if all seven K levels were equally populated and were equally pumped. This reduction occurs because of two effects: the unfavorable branching ratios for low- K Q -branch transitions and the greater frequency separation of the rovibrational transitions in the IR than the associated rotational transitions in the THz. For these same reasons, all other transitions have larger $\Pi(v_j)$ values because their isolated DR signature $\Delta\alpha_j$ is weaker. In other words, at atmospheric pressure, the rovibrational transition that makes the largest contribution to $\Delta\alpha$ is $Q_6(12)$, not $Q_2(12)$ as at low pressure [Fig. 4(a)].

At atmospheric pressure, the $9P(20)$ line also excites other rovibrational transitions besides the $Q_K(12)$ series, namely, $Q_{13}(13)$ and $P_0(1)$ [Fig. 5(a)]. These are quite weak because of

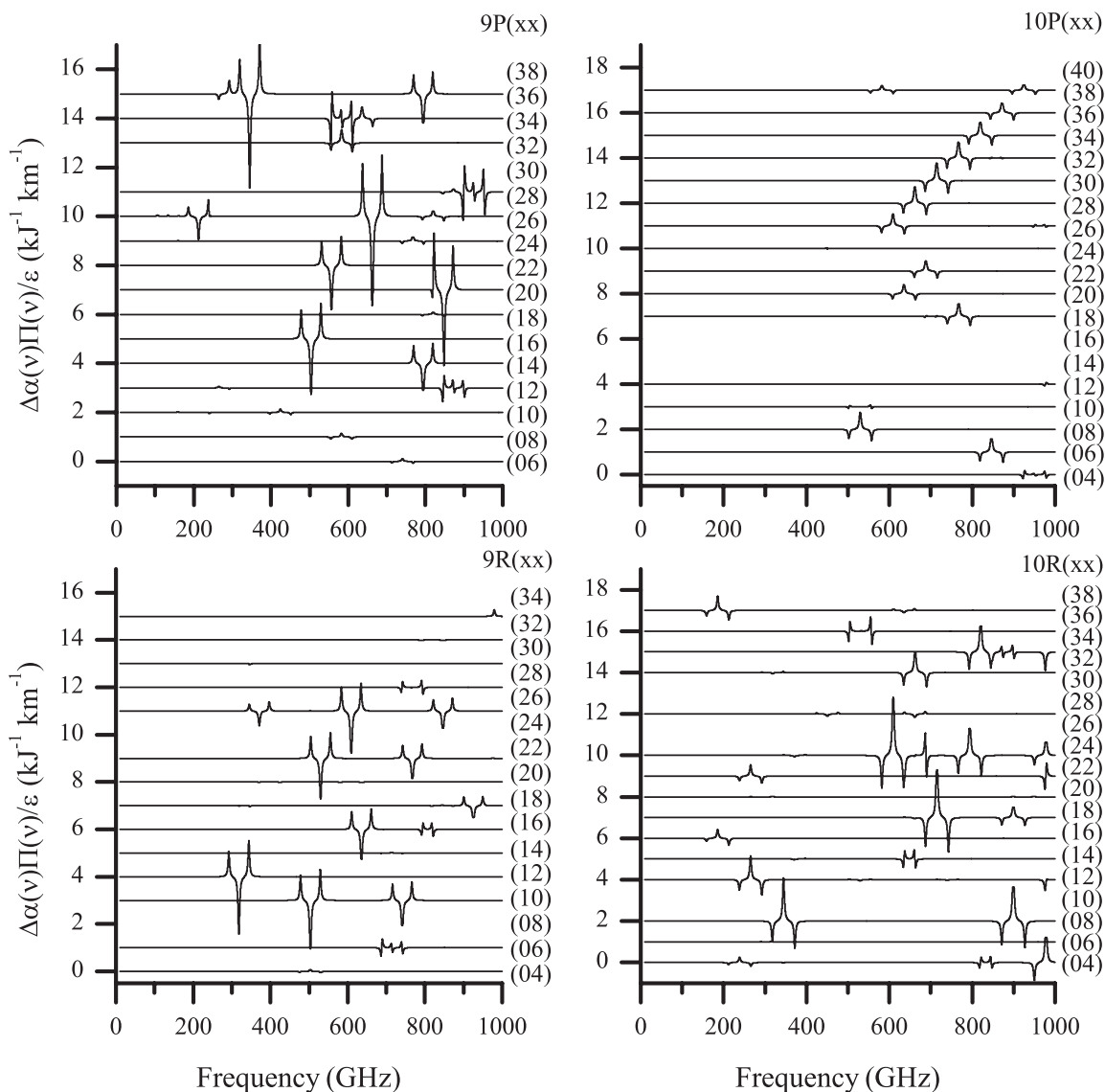


FIG. 6. Calculated DR signatures for all laser coincidences with $\text{CH}_3^{35}\text{Cl}$. The coincident CO_2 laser lines are listed on the right.

the low thermal population in the respective (J_p, K_p, V_0) states. Laser lines adjacent to $9P(20)$ also produce new coincidences, but the DR signatures are weaker [Fig. 5(a)]. This suggests a trend that becomes more obvious when CH_3Cl is studied: The overlap of rovibrational transitions and CO_2 laser lines can be likened to a moiré pattern formed by two overlapping grids with slightly varying spatial frequencies. Overlaps more often come in clusters of CO_2 laser lines instead of through random isolated lines.

P - and R -type rovibrational transitions also manifest four THz DR components, but these occur as a triplet composed of a central doublet flanked by singlets of the opposite sign (Fig. 3). The differing shapes of the P -, Q -, and R -dependent DR spectra, particularly, the associated $\Delta\alpha_j$ sign differences, represent an additional degree of recognition specificity at a specific THz probe frequency. A typical example of a R -branch DR signature comes from the $R_3(4)$ transition in $^{13}\text{CH}_3\text{F}$, optically pumped by the $9P(32)$ line of a CO_2 laser [Fig. 5(b)]. A P -branch DR signature would be identical except flipped in

sign. The central doublet consists of two components of the same sign separated by $\nu \sim 2(B_3 - B_0)(J + 1) = 3.4$ GHz, whereas, the singlets of opposite sign are separated from the doublets by $\nu \sim 2B \approx 50$ GHz. Consequently, the DR signature is spread twice as far in frequency as Q -branch DR signatures. The central doublet is barely resolved and very strong at atmospheric pressure.

It is striking how sparse the THz DR spectra are in Figs. 5(a) and 5(b). Although $^{12}\text{CH}_3\text{F}$ and $^{13}\text{CH}_3\text{F}$ have 13 and 22 pressure-broadened coincidences, respectively, most of them occur in clusters of adjacent rovibrational transitions of constant J but varying K excited by the same laser line. Consequently, there are only five and two distinguishable coincidences for $^{12}\text{CH}_3\text{F}$ and $^{13}\text{CH}_3\text{F}$, respectively, each of which has up to four frequency-resolvable THz DR components. No CO_2 laser line that excites one isotopomer excites the other. There are no DR signatures of one isotopomer within the same $2\Delta\nu_P \approx 5$ -GHz window of any DR signature from the other isotopomer. Indeed, the recognition specificity matrices

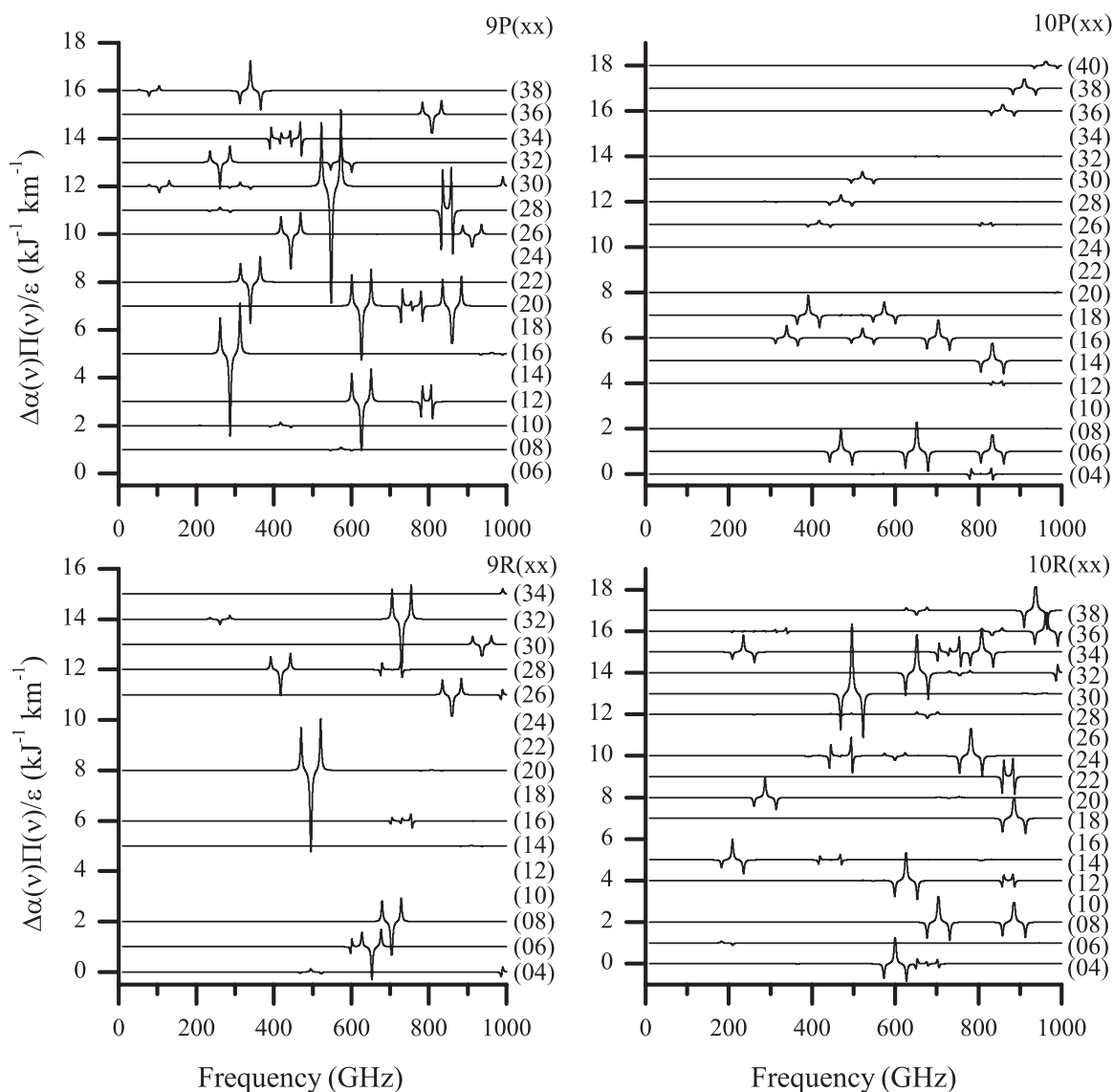


FIG. 7. Calculated DR signatures for all laser coincidences with $\text{CH}_3^{37}\text{Cl}$. The coincident CO_2 laser lines are listed on the right.

of $^{12}\text{CH}_3\text{F}$ and $^{13}\text{CH}_3\text{F}$ are so sparse that the isotopomers are easily distinguished through the selection of the CO_2 laser line and corresponding THz probe frequency.

B. Generalizations to other molecules

To explore how general a result this is for stretching mode DR spectra, consider more massive or complex prolate molecules and their correspondingly smaller rotational constants. Because individual absorption strengths α_{THz} will weaken with increasing molecular mass and rotational partition function, the correspondingly reduced n_L and α_{IR} might also be expected to weaken the DR signals $\Delta\alpha_j\Pi(v_j)/\varepsilon$. However, the number of rovibrational IR coincidences and rotational state overlaps $[\Pi(v_j)]$ increase with increasing molecular mass and complexity because the rotational spacings shrink and the peak THz absorption redshifts. These effects partially or completely compensate for the increased partition function and reduced n_L . The increasing number of

coincidences with CO_2 laser lines will also add more elements to the recognition specificity matrix, permitting selection of favorable DR features in atmospheric transmission windows. Nevertheless, the specificity matrix is very large, containing approximately $60 \times 200 \times 2 = 24\,000$ unique combinations of sixty CO_2 laser frequencies, two hundred 5-GHz-wide windows from 0 to 1 THz, and \pm sign of $\Delta\alpha_j$, respectively. Only in the rarest of cases when two molecules excited by the same laser line and produce a DR signal of the same sign in the same 5-GHz-wide window will this affect the distinguishability of molecules through their DR signatures. Such false positive detections can be avoided by simply photoexciting a different coincidence.

The challenge of multiple coincidences requires a strategy for identifying the strongest DR signature. Several insights from the analysis of CH_3F arise. All isotopomers (and their isotopic abundances) must be considered when identifying the strongest DR signature for a given molecule. In the case of methyl fluoride, the largest $\Delta\alpha_j\Pi(v_j)/\varepsilon$ for the photoexcited

R -branch rovibrational transitions of $^{13}\text{CH}_3\text{F}$ is seven times larger than the strongest Q -branch-excited values in $^{12}\text{CH}_3\text{F}$. Only ^{13}C 's rarity (1% isotopic abundance) prevents $^{13}\text{CH}_3\text{F}$ from being the preferred isotopomer.

Next, consider the factor $|\langle U | \frac{d\mu}{dQ} | L \rangle|^2$ in $\Delta\alpha_j \Pi(v_j)/\varepsilon$ for these rovibrational transitions, which may be expressed as the product of $(d\mu/dQ)^2$ and the quantum-mechanical branching ratios in Table II. Because of the latter, Q -branch transitions are only favored when $J \approx K$. However, levels with $J \approx K$ have the weakest thermal rotational population, and these same branching ratios dramatically weaken the corresponding $\Delta J = 1$ DR signatures. For a given K , the branching ratio for Q -branch transitions tends to zero as J increases, whereas, P - and R -branch transitions tend to $\frac{1}{2}$. Because low- K transitions have closer THz spectral spacing and comparatively larger thermal populations than high- K transitions, it is evident that photoexciting low- K P - or R -branch transitions will yield the largest Π_R enhancement factors.

Other factors also favor P - and R -branch transitions over the Q branch. It has already been mentioned that the strongest DR signatures arise when transitions near the peaks of the IR spectra are excited. For increasingly massive molecules, the rotational quantum numbers J associated with these peaks will increase, and the rotational constants B and their differences ($B_i - B_0$) will decrease. Now, consider again the $2(B_3 - B_0)(J + 1)$ spacings of the doublets in the respective transitions (ignoring higher-order distortion terms) as illustrated in Fig. 3. In general, features are resolvable when $2(B_3 - B_0)(J + 1) > \Delta\nu_P$. In P - and R -branch transitions, the doublet components have the same sign of $\Delta\alpha$, so decreasing $(B_3 - B_0)$ or J simply increases the overlap and effectively doubles the strength of the central doublet. By contrast, the doublet components in Q -branch transitions have opposite signs, so decreasing $(B_3 - B_0)$ or J can weaken the doublet to the point of disappearance. This explains why Q -branch transitions often have DR signatures for which $\Pi(v_j)$ is less than 1 and, more importantly, suggests that P - and R -branch transitions are more resilient than Q -branch transitions to the trade-off between decreasing $(B_i - B_0)$ and increasing J .

Summarizing our findings to this point, the strongest DR signatures involving vibrational stretching modes will be obtained when photoexciting rotational transitions with low K whose J values correspond to P - or R -branch rovibrational transitions near the peak of the corresponding IR spectra. Although these rules were derived for symmetric top molecules, their extension to the stretching modes of other types of molecules is straightforward and is simplified by the fact that many of the asymmetric rotor distortions and hyperfine splittings are unresolved within the pressure-broadened linewidth of the DR signal. These transitions constitute the “overlap enhancement factor” $\Pi(v_j)$ for asymmetric rotors.

C. Methyl chloride

Turning now to CH_3Cl , the calculated THz DR spectra in Figs. 6 and 7 reveal that both isotopomers, $\text{CH}_3^{35}\text{Cl}$ and $\text{CH}_3^{37}\text{Cl}$, exhibit many more coincidences than in CH_3F . Although it is true that the B rotational constant is roughly half that in CH_3F (13.3 GHz for CH_3Cl , 25.5 GHz for CH_3F), that fact alone should only double the number of DR signatures

over CH_3F . Instead, $\text{CH}_3^{35}\text{Cl}$ and $\text{CH}_3^{37}\text{Cl}$ have 154 and 140 coincidences within one atmospheric pressure-broadened linewidth, respectively, seven to ten times more than CH_3F .

The difference is caused by the fact that the laser is now coincident with the V_6 vibrational bending level rather than the V_3 stretching level. Because bending modes ($l = \pm 1$) couple vibrational and rotational (K) motion to produce l -doubled spectra, the selection rules and branching ratios in Table III produce much richer rovibrational, rotational, and THz DR spectra (Figs. 1, 6, 7). In particular, the $\pm K$ degeneracy is removed by large energies that are proportional to Kl , and rovibrational transitions connect states of quantum number K in V_0 with states of quantum number $(K - l)$ in V_6 . Besides doubling the number of rotational and rovibrational transitions, l doubling introduces large energy and frequency splittings in V_6 , so fewer rovibrational transitions occur within an atmospheric pressure-broadened linewidth. Indeed, atmospheric pressure broadening never adds coincidences in CH_3Cl with adjacent rovibrational transitions that preserve J but change K for a given laser line, in stark contrast with CH_3F .

Instead, it is often found that a given laser line photoexcites a complex combination of overlapping and nonoverlapping P -, Q -, and/or R -branch transitions simultaneously, typically involving widely separated rotational states and THz transition frequencies (see Figs. 6 and 7). The DR signature can be understood as a collection of these individual P -, Q -, and R -branch DR signatures (Fig. 3) whose strengths and frequencies vary widely based on the idiosyncrasies of the constituent rotational quantum numbers, energies, and transition branching ratios. The aggregate DR spectrum for a given laser line is quite unique, providing additional specificity.

For example, consider the $9P(26)$ laser line, which has a known low-pressure coincidence with the $^R Q_3(6)$ rovibrational transition in $\text{CH}_3^{35}\text{Cl}$ [Fig. 4(b)]. At atmospheric pressure, nine more P -, Q -, and R -branch rovibrational transitions are photoexcited, including the entire Q -branch sequence from $^R Q_3(4)$ to $^R Q_3(8)$, plus $^R R_2(7)$, $^R P_4(8)$, $^R R_0(24)$, $^P R_0(24)$, and $^R P_7(31)$, producing DR spectra that span 106–848 GHz. Interestingly, the strongest of these features are not those associated with the known low pressure $^R Q_3(6)$ coincidence but with the new $^R R_0(24)$ coincidence. A contributing reason for this is the increased overlap of the opposite sign Q -branch doublets spaced $2(B_i - B_0)(J + 1)$ apart: $(B_6 - B_0) \approx 49$ MHz in CH_3Cl while $(B_3 - B_0) \approx 339$ MHz in CH_3F . Although the coincidences in CH_3Cl typically involve states with larger J than CH_3F , atmospheric pressure broadening causes the Q -branch doublets to overlap strongly enough to reduce $\Pi(v_j)$ below 1 in most cases.

Comparing the relative strengths of the constituent transitions excited by the $9P(26)$ line provides helpful insight into the subtle interplay of factors that contribute to the complex DR signature. First of all, because the laser frequency is within one pressure-broadened linewidth of all ten coincident IR transitions, the strength of the corresponding DR signatures depends primarily on the branching ratio of the transition. Table III indicates that, as $K \rightarrow J$, the IR transitions $^R R$ and $^P P$ grow much stronger than the $^P R$ and $^R P$ transitions. For example, the branching ratios of the IR transitions $^R R_2(7)$ and $^R P_4(8)$ are 0.229 and 0.022, respectively, explaining why their contributions to the DR signature differ by an order of

TABLE VI. Abbreviated table of atmospheric pressure DR parameters for CH₃³⁵Cl. The complete table may be found in Ref. [39].

Laser line	IR transition	IR transition offset (GHz)	R_0^-	R_0^+	R_i^-	R_i^+
			ν_j (GHz)	ν_j (GHz)	ν_j (GHz)	ν_j (GHz)
			$\Delta\alpha(\nu_j)/\epsilon$ (km ⁻¹ kJ ⁻¹)			
			$\Pi(\nu_j)$	$\Pi(\nu_j)$	$\Pi(\nu_j)$	$\Pi(\nu_j)$
9P(26)	$^R Q_3(4)$	1.09	106.324	132.902		132.416
			0.072	-0.128		0.072
			1.008	-0.500		0.763
$^R Q_3(5)$	0.60		132.902	159.477	132.416	158.894
			0.263	-0.364	-0.148	0.268
			0.243	-0.150	-0.371	0.136
$^R Q_3(6)$	0.02		159.477	186.050	158.894	185.370
			0.533	-0.669	-0.394	0.550
			0.102	-0.676	-0.092	0.724
$^R R_2(7)$	-1.28		186.064	212.636	211.858	238.329
			0.457	-0.528	-0.482	0.557
			0.990	1.709	1.825	0.951
$^R Q_3(7)$	-0.66		186.050	212.620	185.370	211.843
			0.760	-0.905	-0.624	0.787
			0.595	0.998	-0.637	-1.115
$^R Q_3(8)$	-1.44		212.620	239.187	211.843	238.312
			0.815	-0.942	-0.709	0.847
			-1.108	-0.244	1.238	0.630
$^R P_4(8)$	0.69		212.598	239.162	185.351	211.821
			0.041	-0.049	-0.024	0.033
			-22.055	-4.862	-16.765	-26.324
$^R R_0(24)$	1.04		637.057	663.512	661.071	687.418
			2.316	-2.410	-2.397	2.491
			0.970	1.425	1.430	0.971
$^P R_0(24)$	1.13		637.057	663.512	661.075	687.422
			2.244	-2.335	-2.323	2.414
			1.001	1.471	1.476	1.002
$^R P_7(31)$	-0.31		821.399	847.750	792.123	818.390
			0.162	-0.168	-0.153	0.159
			1.345	0.988	0.986	1.359

magnitude [Fig. 4(b)]. Likewise, the $^R Q_K(J)$ branching ratios (Table III) tend to zero as $J \rightarrow K$, so inspection of the Q -branch series $^R Q_3(4)$ to $^R Q_3(8)$ in Fig. 4(b) reveals the V_6 contributions to the Q -branch doublets disappear as J decreases.

Figures 6 and 7 suggest the strongest DR feature for almost every coincidence derives from photoexcitation of a P - or R -branch transition. Although laser coincidences usually occur with isolated P - or R -branch transitions, sometimes a sequence of laser lines coincides with a sequence of IR transitions. A prominent example involves the series of laser lines spanning $10P(26)$ – $10P(38)$ where coincidences that preserve $K = 9$ for odd J span $^P P_9(23)$ – $^P P_9(35)$, one per laser line. Many shorter sequences with this same moiré like overlap pattern of preserving K but changing J were found in both isotopomers.

By contrast, Q -branch transitions cluster strongly, so multiple IR transitions may be excited by a single laser line. Unlike V_3 of CH₃F for which the P -, Q -, and R -branch IR transitions are arranged in clusters that preserve J for all K [Fig. 1(b)], l doubling in V_6 of CH₃Cl spreads out the Q -branch transitions into clusters that preserve K for all J [Fig. 1(c)]. Consequently, a given CO₂ laser line may

excite many such J -changing K -preserving IR transitions, explaining how the $9P(26)$ line excites $^R Q_3(4)$ – $^R Q_3(8)$. When this occurs, an additional reduction in the DR signature occurs. Recall that the spacing of the transitions and the separation of the Q -branch components of opposite sign are both $\sim 2B$. As a result, the positive component of one DR feature overlaps the negative component of the preceding DR feature [Fig. 4(b)], and the summed Q -branch DR signature is much weaker than its constituent components. Therefore, Q -branch transitions generally produce unfavorably weak DR features for bending vibrational modes, just as they did in stretching vibrational modes, but for different reasons.

So atmospheric pressure broadening typically produces overlapping sequences of Q -branch DR features with $\Pi(\nu_j) < 1$ and isolated P - and R -branch DR features with $1 < \Pi(\nu_j) < 2$. However, inspection of Table VI indicates that $\Pi(\nu_j)$ can sometimes be much larger. For example, $\Pi(\nu_j) \approx 25$ for the two DR signatures near 212 GHz associated with the $^R P_4(8)$ transition. Such $\Pi(\nu_j) > 2$ cases are not caused by the summation of overlapping DR signatures excited by a single IR transition as is the case for CH₃F. Instead, these are rare instances in which very different rovibrational transitions excited by the

same laser line produce THz DR signatures that coincidentally overlap. In the example at 212 GHz, the weak ${}^R P_4(8)$ DR signatures overlap with DR signatures 17 and 5 times stronger produced by the ${}^R R_2(7)$ and ${}^R Q_3(8)$ transitions, respectively.

The increased mass of $\text{CH}_3 {}^{37}\text{Cl}$ lowers the vibrational energy of V_6 , so the DR spectra of $\text{CH}_3 {}^{37}\text{Cl}$ are similar in form but different in detail to those of $\text{CH}_3 {}^{35}\text{Cl}$. The isotopic abundances (76% and 24% for ${}^{35}\text{Cl}$ and ${}^{37}\text{Cl}$, respectively) suggest that $\text{CH}_3 {}^{35}\text{Cl}$ will be the preferred isotopomer for remote sensing. However, if a DR signature from $\text{CH}_3 {}^{37}\text{Cl}$ is three times stronger than any from $\text{CH}_3 {}^{35}\text{Cl}$, the less abundant isotope could produce the strongest DR signature. Indeed, if we constrain ourselves to look at the region of greatest practical interest below 300 GHz and to account for isotopic abundances, we find that the strongest DR signature for CH_3Cl is the ${}^R R_3(10)$ transition of $\text{CH}_3 {}^{37}\text{Cl}$ at 287 GHz excited by the $9P(16)$ laser line.

IV. CONCLUSIONS

Our analysis has shown the potential of IR-THz DR spectroscopy for the remote recognition of a trace gas in the atmosphere given sufficient pump intensity and gas concentration. Discrimination comes from the two dimensions of a sparse recognition specificity matrix derived from (1) the few coincidences that occur between CO_2 pump laser lines and rovibrational transitions of the analyte and (2) the unique changes in THz absorption the pump coincidences induce. The strength of the DR signature depends sensitively on the type of rovibrational transition excited by the laser coincidence and the quantum and statistical mechanics of the involved transitions.

Atmospheric pressure broadening, which smears out transitions detected with traditional THz spectroscopic techniques, actually assists the IR-THz DR technique by providing more pump coincidences and more overlapping transitions for a given coincidence. These advantages allow an optimal DR signature to be selected for a given analyte, and it was shown how to calculate this from basic molecular parameters.

Generally speaking, the DR signatures for CH_3Cl are much weaker than those for CH_3F : The transition dipole moments are smaller, and the rotational partition function is larger, so the rovibrational pump absorption coefficient is weaker. Weak IR absorption, particularly for molecules whose pump coincidences involve bending modes, presents the greatest challenge to DR spectroscopy, just as it has limited the performance of many optically pumped far-infrared laser gases. For heavier molecules, this problem may be alleviated as the transition dipole moments tend to increase (e.g., $d\mu/dQ_6 = 0.054$ D for CH_3Br), and increasing complex vibrational energy-level structures allow some selection in which vibrational mode the laser excites (e.g., a CO_2 laser may excite the V_4 , V_7 , or $3V_8^1$ vibrational modes of CH_3CN) [32,33].

ACKNOWLEDGMENTS

The authors gratefully acknowledge the support and scientific discussions with J. Holt, I. Medvedev, C. Neese, P. Helminger, and D. Petkie. This work was partially supported by the Army's competitive in-house innovative laboratory program, the Defense Threat Reduction Agency (Contract No. HDTRA1-09-1-0031) and DARPA.

-
- [1] A. Othonos, *Appl. Phys. Rev.* **83**, 1789 (1998).
 - [2] D. Rosen, A. G. Doukas, Y. Budansky, A. Katz, and R. R. Alfano, *Appl. Phys. Lett.* **39**, 935 (1981).
 - [3] J. Shah, *Ultrafast Spectroscopy of Semiconductors and Semiconductor Nanostructures* (Springer, Berlin, 1999).
 - [4] A. Hoge, C. Galland, M. Winger, and A. Imamoglu, *Phys. Rev. Lett.* **100**, 217401 (2008).
 - [5] J. C. Petersen and J. Hald, *Opt. Express* **18**, 7955 (2010).
 - [6] J. O. Henningsen and J. C. Petersen, *J. Opt. Soc. Am. B* **5**, 1848 (1988).
 - [7] P. A. George, J. Strait, J. Dawlaty, S. Shivaraman, M. Chandrashekhara, F. Rana, and M. G. Spencer, *Nano Lett.* **8**, 4248 (2008).
 - [8] H. O. Everitt and F. C. De Lucia, in *Advances in Atomic, Molecular, and Optical Physics*, edited by B. Bederson and H. Walther (Academic, San Diego, 1995).
 - [9] C. Callegari, I. Reinhard, K. K. Lehmann, G. Scoles, K. Nauta, and R. E. Miller, *J. Chem. Phys.* **113**, 4636 (2000).
 - [10] U. Merker, H. K. Srivastava, A. Callegari, K. K. Lehmann, and G. Scoles, *PhysChemChemPhys* **1**, 2427 (1999).
 - [11] T. Shimizu and T. Oka, *Phys. Rev. A* **2**, 1177 (1970).
 - [12] T. Y. Chang and T. J. Bridges, *Opt. Commun.* **1**, 249 (1970).
 - [13] *Handbook of Laser Wavelength*, edited by M. J. Weber (CRC, Boca Raton, FL, 1999).
 - [14] G. Dodel, *Infrared Phys. Technol.* **40**, 127 (1999).
 - [15] W. H. Matteson and F. C. De Lucia, *IEEE J. Quantum Electron.* **19**, 1284 (1983).
 - [16] H. O. Everitt, D. D. Skatrud, and F. C. De Lucia, *Appl. Phys. Lett.* **49**, 995 (1986).
 - [17] R. I. McCormick, H. O. Everitt, F. C. De Lucia, and D. D. Skatrud, *IEEE J. Quantum Electron.* **23**, 2069 (1987).
 - [18] R. L. Crownover, H. O. Everitt, F. C. De Lucia, and D. D. Skatrud, *Appl. Phys. Lett.* **57**, 2882 (1990).
 - [19] S.-L. Chua, C. A. Caccamise, D. J. Phillips, J. D. Joannopoulos, M. Soljacic, H. O. Everitt, and J. Bravo-Abad, *Opt. Express* **19**, 7513 (2011).
 - [20] T. W. Pape, F. C. De Lucia, and D. D. Skatrud, *J. Chem. Phys.* **100**, 5666 (1994).
 - [21] F. C. De Lucia, D. T. Petkie, and H. O. Everitt, *IEEE J. Quantum Electron.* **45**, 163 (2009).
 - [22] J. O. Hirschfelder, C. F. Curtiss, and R. B. Bird, *Molecular Theory of Gases and Liquids* (Wiley, New York, 1954).
 - [23] W. J. Witteman, *The CO_2 Laser* (Springer-Verlag, New York, 1987).
 - [24] C. H. Townes and S. L. Schawlow, *Microwave Spectroscopy* (Dover, New York, 1975).
 - [25] Q. Song and R. H. Schwendeman, *J. Mol. Spectrosc.* **165**, 277 (1994).

- [26] J.-C. Deroche and G. Graner, in *Optically Pumped Far-Infrared Lasers*, edited by K. J. Button, M. Inguscio, and F. Strumia (Plenum, New York, 1984).
- [27] W. Gordy and R. L. Cook, *Microwave Molecular Spectra* (Wiley, New York, 1970).
- [28] P. F. Bernath, *Spectra of Atoms and Molecules* (Oxford University Press, New York, 2005).
- [29] G. Blanquet, J. L. Walrand, and M. Dang-Nhu, *J. Mol. Spectrosc.* **159**, 156 (1993).
- [30] G. Tarrago, O. N. Ulenikov, and G. Poussigue, *J. Phys. (France)* **45**, 1429 (1984).
- [31] D. Papousek, Z. Papouškova, and D. P. Chong, *J. Phys. Chem.* **99**, 15387 (1995).
- [32] A.-M. Tolonen, M. Koivusaari, R. Paso, J. Schroderus, S. Alanko, and R. Anttila, *J. Mol. Spectrosc.* **160**, 554 (1993).
- [33] H. Sarkkinen, R. Paso, and R. Anttila, *Infrared Phys. Technol.* **137**, 643 (1996).
- [34] D. Papousek, J. F. Ogilvie, S. Civis, and M. Winnewisser, *J. Mol. Spectrosc.* **149**, 109 (1991).
- [35] D. Papousek, J. Demaison, G. Wlodarczak, P. Pracna, S. Klee, and M. Winnewisser, *J. Mol. Spectrosc.* **164**, 351 (1994).
- [36] D. Papousek, R. Tesar, P. Pracna, J. Kauppinen, S. P. Belov, and M. Y. Tretyakov, *J. Mol. Spectrosc.* **146**, 127 (1991).
- [37] M.-F. Le Moal, M. Margottin-Maclou, and A. Valentin, *J. Mol. Spectrosc.* **183**, 93 (1997).
- [38] S. W. Sharpe, T. J. Johnson, R. L. Sams, P. M. Chu, G. C. Rhoderick, and P. A. Johnson, *Appl. Spectrosc.* **58**, 1452 (2004).
- [39] D. J. Phillips, E. A. Tanner, F. C. De Lucia, and H. O. Everitt, e-print [arXiv:1202.0595v2](https://arxiv.org/abs/1202.0595v2).